A solar wind-derived water reservoir on the Moon hosted by impact glass beads

Huicun He [1,2], Jianglong Ji [1,2], Yue Zhang[3], Sen Hu [1,2] ✉, Yangting Lin [1,2], Hejiu Hui [3,4] ✉, Jialong Hao [1], Ruiying Li [1], Wei Yang [1,2], Hengci Tian [1,2], Chi Zhang [1,2], Mahesh Anand [5,6], Romain Tartèse [7], Lixin Gu [1], Jinhua Li [1,2], Di Zhang [8], Qian Mao[8], Lihui Jia [8], Xiaoguang Li [8], Yi Chen [8], Li Zhang[9,4], Huaiwei Ni[9,4], Shitou Wu [8], Hao Wang [8], Qiuli Li [8], Huaiyu He[8], Xianhua Li [8] & Fuyuan Wu [8]

The past two decades of lunar exploration have seen the detection of substantial quantities of water on the Moon's surface. It has been proposed that a hydrated layer exists at depth in lunar soils, buffering a water cycle on the Moon globally. However, a reservoir has yet to be identified for this hydrated layer. Here we report the abundance, hydrogen isotope composition and core-to-rim variations of water measured in impact glass beads extracted from lunar soils returned by the Chang'e-5 mission. The impact glass beads preserve hydration signatures and display water abundance profiles consistent with the inward diffusion of solar wind-derived water. Diffusion modelling estimates diffusion timescales of less than 15 years at a temperature of 360 K. Such short diffusion timescales suggest an efficient water recharge mechanism that could sustain the lunar surface water cycle. We estimate that the amount of water hosted by impact glass beads in lunar soils may reach up to 2.7×10^{14} kg. Our direct measurements of this surface reservoir of lunar water show that impact glass beads can store substantial quantities of solar wind-derived water on the Moon and suggest that impact glass may be water reservoirs on other airless bodies.

It has long been argued that there could be water and other volatile species at the surface of the Moon[1–3]. Renewed lunar exploration and advances in remote-sensing measurements in the late 1990s allowed the neutron spectrometer on board the Lunar Prospector mission to confirm the existence of water ice at the lunar poles[4]. Following this, the Moon mineralogy mapper instrument on board the Chandrayaan-1 spacecraft detected the diagnostic absorption bands of hydroxyl and/or water at 2.8–3.0 μm on the surface of the Moon[5]. Detailed analyses indicated that hydroxyl/water could be present all over the Moon's surface, which also displayed temporal and spatial variations, with equivalent water abundances ranging between ~10 and 1,000 μg g^{-1} (refs. [6–10]). Furthermore, the Lunar Crater Observation and Sensing Satellite impact experiment carried out in 2009 provided direct evidence for high water-ice abundances (5.6 ± 2.9 wt%) in permanently

[1]Key Laboratory of Earth and Planetary Physics, Chinese Academy of Sciences, Beijing, China. [2]University of Chinese Academy of Sciences, Beijing, China. [3]State Key Laboratory for Mineral Deposits Research and Lunar and Planetary Science Institute, School of the Earth Sciences and Engineering, Nanjing University, Nanjing, China. [4]CAS Center for Excellence in Comparative Planetology, Hefei, China. [5]School of Physical Sciences, The Open University, Milton Keynes, UK. [6]Department of Earth Sciences, The Natural History Museum, London, UK. [7]Department of Earth and Environmental Sciences, The University of Manchester, Manchester, UK. [8]State Key Laboratory of Lithospheric Evolution, Chinese Academy of Sciences, Beijing, China. [9]School of Earth and Space Sciences, University of Science and Technology of China, Hefei, China. ✉e-mail: husen@mail.iggcas.ac.cn; hhui@nju.edu.cn
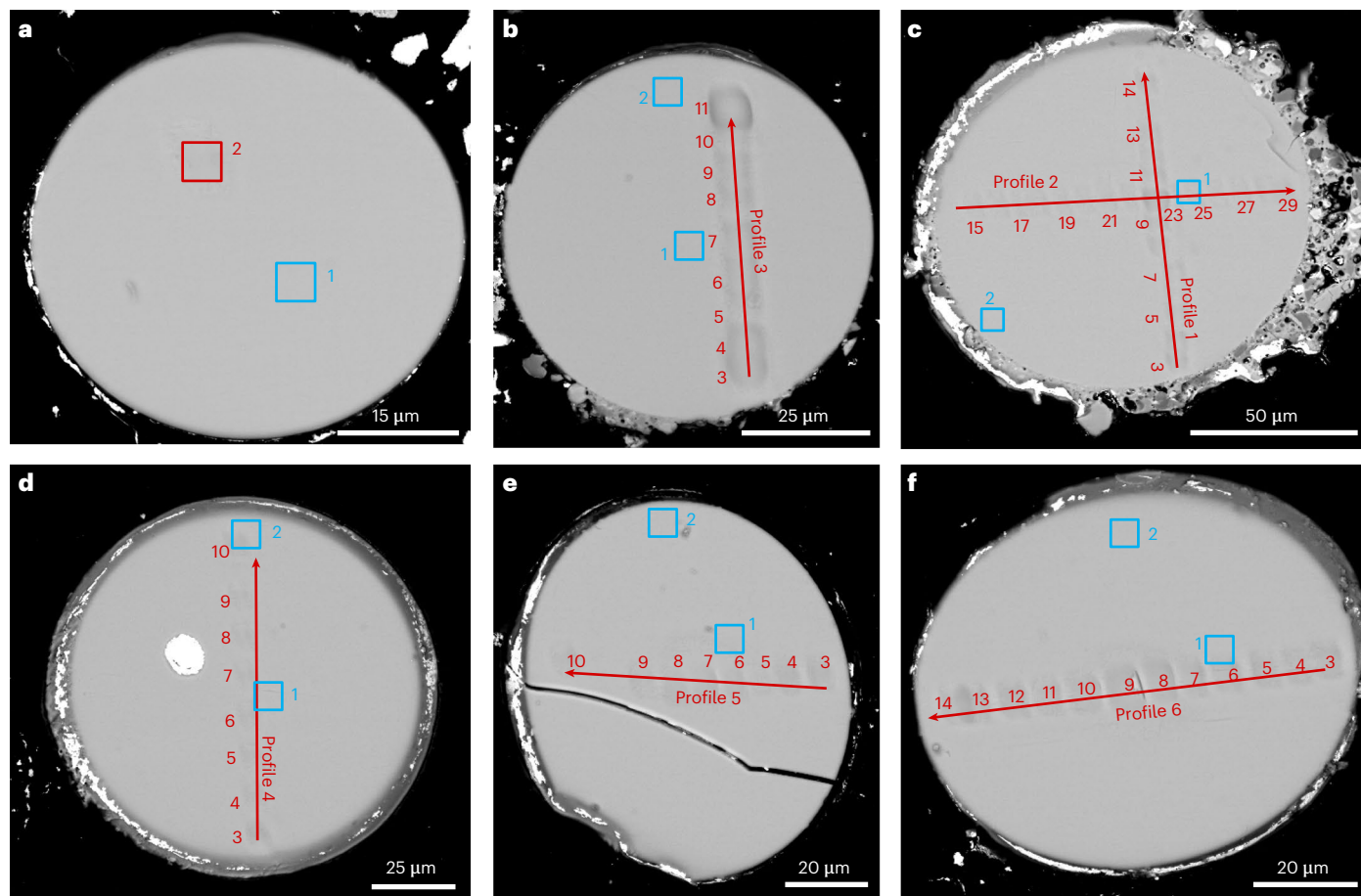
Fig. 1 | Representative back-scattered electron images of CE5 impact glass beads after nanoSIMS analyses. a, CE5#33,002. **b**, CE5#33,003. **c**, CE5#33,036. **d**, CE5#33,046. **e**, CE5#33,052. **f**, CE5#33,076. These impact glass beads have spherical shapes and have homogeneous chemical compositions (Supplementary Table 2). Beads CE5#33,003 and CE5#33,036 are coated by finer agglutinates. Six profiles carried out on five impact glass beads in the second session are outlined in red. Blue squares indicate locations of NanoSIMS in the first analytical session. Each NanoSIMS analysis pit is 7 × 7 μm².

shadowed regions within Cabeus crater[11]. Elevated water-ice abundance in lunar polar regions was further supported by the neutron flux measurements performed by the Lunar Exploration Neutron Detector on board the Lunar Reconnaissance Orbiter spacecraft[12]. Recently, the neutral mass spectrometer on the Lunar Atmosphere and Dust Environment Explorer detected exospheric water liberated by meteoroid impacts[13], and ground-based telescope observations detected molecular water on the lunar surface[14]. Today, there is little doubt that most of the Moon's surface harbours water in one form or another. However, the origin(s) of this lunar surface water and its spatial distribution and evolution during regolith gardening remain largely unknown, despite key implications for future lunar surface exploration and for better understanding the (sub)surface water reservoir and processing on Solar System airless bodies.

There are several potential sources and processes that could have contributed to the water inventory at the surface of the Moon[15], such as (1) solar wind implantation[16–20], (2) outgassing of volatiles during lunar volcanism[21–23], (3) deposition of volatile-bearing pyroclastic deposits[24] and minerals[25] and (4) delivery by impacts of comets and asteroids[26–29]. It is generally thought that solar wind hydrogen-ion implantation could react with surface minerals to produce hydroxyl or water in lunar soils[30,31]. The surface water produced and/or delivered on the Moon's equatorial regions may migrate to polar regions, driven by temperature oscillations[16,19,32,33], and could also be partially released to space[13]. Hence, a scenario of lunar water cycle was further proposed to describe the retention, release and replenishment of water on the

surface of the Moon[13]. To sustain a water cycle at the surface of the Moon, there should be a hydrated layer (reservoir) at depth in lunar soils[13]. However, finding this water reservoir has remained elusive, despite several studies having investigated the water inventory of fine mineral grains in lunar soils (for example, refs. [34,35]), impact-produced agglutinates[27], volcanic rocks (for example, ref. [26]) and pyroclastic glass beads[21,36]. Consequently, there must be a yet-unidentified water reservoir in lunar soils that has the capacity to buffer a lunar surface water cycle.

The lunar soils returned by the Apollo, Luna and Chang'e-5 (CE5) missions comprise mainly rock and mineral fragments, pyroclastic glass beads, impact-produced agglutinates and impact glass beads[37,38]. Among these components, the water inventory of impact glass beads has not yet been investigated in detail, despite these glassy beads being potential candidates for playing a significant role in a lunar surface water cycle. To investigate this possibility, we carried out a systematic characterization of the petrography, major element composition, Raman characteristics, water abundance and hydrogen isotope composition on the impact glass beads returned by the CE5 mission, aiming to identify and characterize the missing water reservoir on the Moon's surface. A recent geochronological study of CE5 impact glass beads has shown that they formed more or less continuously for the past 2 Gyr, with prominent peaks in formation ages at ~575 million years ago (Ma), 380 Ma, 68 Ma and 35 Ma, originating predominantly from a few 1- to 5-km-diameter impact craters in the Em4 (Eratosthenian-aged mare) basaltic unit where CE5 landed[39].

Water abundance and hydrogen isotope composition of impact glasses

The studied impact glass beads were hand picked from a lunar soil sample (sample CE5C0100YJFM00103; ~1 g) scooped by the CE5 lander robotic arm. A total of 117 individual spherical glass beads were characterized using field-emission scanning electron microscopy (SEM), electron probe microanalyser (EPMA) and Raman spectroscopy (Fig. 1, Supplementary Figs. 1 and 2, Supplementary Table 1 and Extended Data Fig. 1). Among them, 32 impact glass beads characterized by smooth exposed surfaces and chemical compositions consistent with those of bulk CE5 basalts were chosen for in situ water abundance and H isotope analysis using a nanoscale secondary ion mass spectrometer (NanoSIMS) (Fig. 1, Extended Data Figs. 2 and 3 and Supplementary Table 1). The CE5 impact glass beads contain $0-1,909$ $\mu g\,g^{-1}$ equivalent H_2O, with H isotope compositions (given in delta notation, $\delta D = 1000 \times (D/H_{sample}/D/H_{SMOW}-1)$, where D/H_{sample} is the measured D/H ratio measured in the sample and D/H_{SMOW} is the D/H ratio (1.5576×10^{-4}) of the standard mean ocean water) ranging from $-990 \pm 6‰$ to $522 \pm 440‰$ and which are negatively correlated with the water abundances (Fig. 2). We also analysed water abundances and H isotope compositions along six transects in five glass beads (CE5#33,003, CE5#33,036, CE5#33,046, CE5#33,052 and CE5#33,076; Fig. 1), which show elevated water abundances at the rims that gradually decrease towards the cores while δD values decrease from cores to rims (Fig. 3 and Extended Data Figs. 4 and 5). Three glass beads display sharp decreases in water content from the rims towards the cores, while the other two glass beads display a smoother water abundance variation (Fig. 3 and Extended Data Figs. 4 and 5).

Solar wind origin of water

The rims of CE5 impact glass beads are generally characterized by higher water abundances (up to ~2,000 $\mu g\,g^{-1}$) and lower δD values (~$-990‰$) compared with pyroclastic glasses, impact-produced agglutinates and melt inclusions reported in previous studies (Fig. 2 and Supplementary Table 4). The extremely low δD values measured at the rims of CE5 impact glasses (Fig. 3) are consistent with the H isotope composition of solar wind[40,41]. These low δD values are distinct from other potential lunar water reservoirs, such as indigenous water outgassed during lunar volcanism ($\delta D \approx -300$ to $1,200‰$) (refs. [22,36,42]), water-rich carbonaceous chondrites ($\delta D \approx -200$ to $800‰$) (refs. [43,44]) and comets ($\delta D \approx 0$ to $2,500‰$) (refs. [45,46]), indicating that the water retained in CE5 impact glasses is of a solar wind origin.

There are two potential mechanisms, de-gassing and two-endmember mixing, that could explain the negative correlation between water abundances and δD values defined by CE5 impact glasses (Fig. 2). Because the initial D/H ratio is so low (D/H = 3.1×10^{-6} for the analysis with the highest H_2O abundance), the H_2 de-gassing modelling indicates that D/H fractionation due to H_2 loss would yield an increase in δD values from about $-980‰$ up to only $-926‰$ for 99.9% loss, starting with an initial water abundance in CE5 impact glasses of ~2,000 $\mu g\,g^{-1}$ (Fig. 2 and Methods). Therefore, H_2 loss from CE5 impact glasses via de-gassing is not a viable mechanism to account for the observed δD variations from around $-990‰$ to $+522‰$ (Fig. 2). More important, the high water content at the rim but low water content in the core of the glass beads is not consistent with the de-gassing scenario.

In the other scenario, the CE5 impact glasses could have lost most of the original water inventory of their precursors during their formation at high temperature, following which solar wind-derived water started diffusing inwards into these glass beads on the Moon's surface. This scenario is consistent with the notable lower abundances of volatile elements such as Na_2O (most <0.05 wt%) and K_2O (<0.06 wt%) in CE5 impact glasses compared with CE5 mare basalt fragments ($Na_2O \approx 0.6$ wt% and $K_2O \approx 0.1-0.2$ wt%, on average)[39]. This binary mixing model, between a water-poor but relatively high D/H
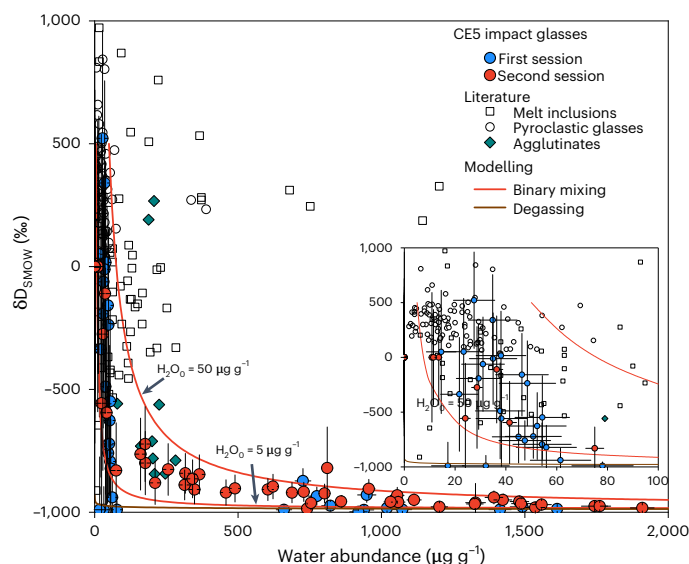

Fig. 2 | Water abundances and δD values measured in CE5 impact glass beads. All glass bead analyses define a negative correlation between the water abundances and δD values, which is consistent with a two-endmember mixing model (red lines) that indicates addition of solar wind-derived water with δD value of $-990‰$ into a low water abundance ($H_2O_0 = 5-50$ $\mu g\,g^{-1}$) CE5 impact glass with δD value of $+500‰$ (ref. [50]). De-gassing of H_2 from CE5 impact glasses cannot be responsible for the large observed $H_2O-\delta D$ variations (brown line). The inset diagram is the zoom-in view of water abundance range of $0-100$ $\mu g\,g^{-1}$. For more details, see Methods. The literature data for melt inclusions, pyroclastic glasses and impact-produced agglutinates are also plotted for comparison, and the datasets are listed in Supplementary Table 4. All error bars correspond to 2 s.d. analytical uncertainties. SMOW, standard mean ocean water. H_2O_0 is the water abundance of impact glass beads prior to the inward diffusion of solar wind-derived water.

endmember and a water-rich but extremely low D/H endmember, reproduces well the range of water abundances and δD values measured in CE5 impact glasses (Fig. 2). Modelling requires that the initial water abundances of CE5 impact glass beads are less than 50 $\mu g\,g^{-1}$ before the addition of solar wind-derived water (Fig. 2). This requirement is consistent with the water abundances measured at the cores of CE5 impact glasses, which are comparable to the instrument H_2O background (~10–30 $\mu g\,g^{-1}$; Methods), indicating that any water potentially present in the precursor materials was lost during formation of the CE5 impact glass beads, before the addition of solar wind-derived water. Most important, the hydration profiles in CE5 impact glass beads show that solar wind-derived water has diffused inwards into the glasses (Fig. 3), unambiguously demonstrating that the addition of solar wind-derived water post-dated the formation of the impact glass beads.

Impact glasses as the driver for the lunar surface water cycle

The negative correlation between water abundances and δD values, coupled with the hydration profiles observed for CE5 impact glass beads, reveal that solar wind-derived water can diffuse into and be stored in lunar impact glasses on the Moon's surface, probably via post-implantation diffusion[19,47]. To model the diffusion timescale, we used Raman spectroscopy to confirm that water hosted in CE5 impact glass beads is in the form of hydroxyl/molecular water (Extended Data Fig. 6). The diffusion coefficient of hydroxyl/water in glasses[48] was used for modelling the duration timescale necessary for forming the observed hydration profiles of CE5 impact glass beads (Methods). Diffusion modelling results indicate that the diffusion time needed
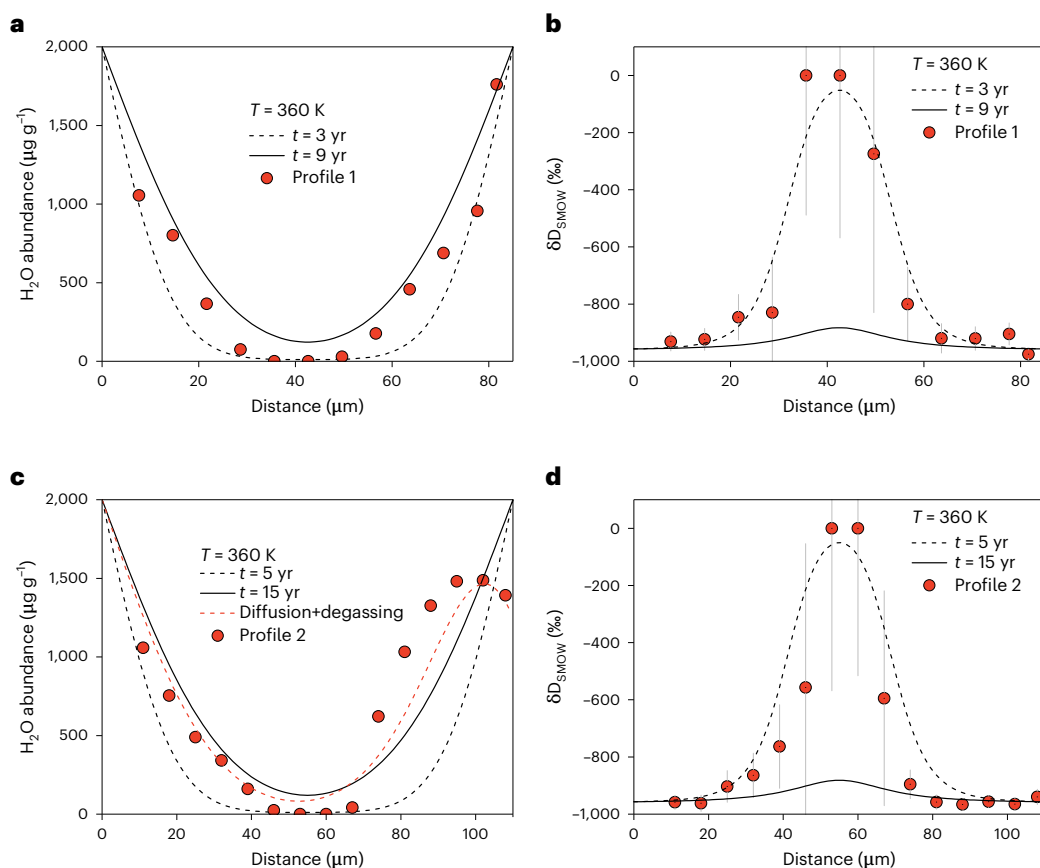
Fig. 3 | Two profiles across CE5 impact glass bead CE5#33,036. a,b, Water abundance (**a**) and δD values (**b**) measured along Profile 1, as outlined in Fig. 1c. **c,d,** Water abundance (**c**) and δD values (**d**) measured along Profile 2, as outlined in Fig. 1c. The apparent distances along the profiles were measured from the rim on a side (Fig. 1c). A water-diffusion coefficient of 20.84 $\mu m^2\,yr^{-1}$ at T = 360 K was used[48]. The maximum diffusion durations for Profile 1 and Profile 2 are 9 and 15 yr at T = 360 K, respectively. Profile 2 was further modelled by a post-diffusion de-gassing on the basis of the bell shape of water abundance on the right side. More modelling details can be found in Methods. All error bars correspond to 2 s.d. analytical uncertainties.

to produce the observed hydration profiles varies from 1 year to 15 years at a peak temperature (T) of 360 K, relevant for the landing site of CE5[32] (Fig. 3, Extended Data Figs. 4 and 5 and Methods). This short diffusion time indicates that the solar wind-derived water can be rapidly accumulated and stored in lunar impact glass beads. It is interesting to note that one profile on bead CE5#33,036 displays notable post-diffusion water loss at the very rim (Fig. 3, and Methods), suggesting that CE5 impact glass beads have the capacity of both incorporating solar wind-derived water and releasing it to the lunar exosphere if T increases. Therefore, we propose that impact glass beads in lunar soils are a prime water reservoir candidate able to drive the lunar surface water cycle (Fig. 4).

Linking a lunar surface water cycle with impact glass beads implies three major processes: (1) formation of impact glass beads, (2) solar wind-derived water implantation and diffusion into the beads and (3) water release to the lunar exosphere during T increase, possibly due to sunlight irradiation and/or meteoroid impacts (Fig. 4). Impact glass beads are produced during melting of lunar soil and regolith targets when impactors hit the Moon. Most of the water present in the precursor materials would have probably been lost during high-temperature melting that led to the formation of the impact glass beads. Solar wind hydrogen ions would then be continually implanted into lunar soils and impact glass beads and would combine with oxygen atoms to form the hydroxyl/water that diffused into the glass interiors and is stored in glass beads. This water stored in impact glass beads could then be released to the lunar exosphere due to sunlight irradiation[19] and/or meteoroid impacts[13].

Some of the CE5 impact glass rims contain higher water abundance (up to ~2,000 $\mu g\,g^{-1}$) than that reported in Apollo agglutinates (<600 $\mu g\,g^{-1}$) (Fig. 2); however, they may still not be water saturated compared with terrestrial basaltic glasses of similar chemical compositions that can contain up to 2.43 wt% H_2O (ref. 49). This could be the result of dynamic diffusion and release of water in the impact glass beads controlled by the time-of-the-day temperature oscillations[10]. The dynamic ingress and egress of water in impact glass beads could have acted as a buffer to explain the global and daily variations of water abundance on the lunar surface and in the lunar exosphere[7,8,10].

Inventory of water in lunar soils

Using the water abundance measured in CE5 impact glass beads and mare basalts[50], we can estimate the relative contribution of solar wind implanted in impact glasses and basalts to the global water inventory in the CE5 regolith. Considering the zoning features of water in CE5 impact glass beads, we estimate that these beads have a bulk water abundance of 132–1,570 $\mu g\,g^{-1}$, which is notably higher than that of the bulk CE5 mare basalts (7 ± 3 $\mu g\,g^{-1}$) (ref. 50). The modal abundance of impact glass beads in lunar soils is in the region of 3–5 vol.% estimated from Apollo lunar soils[51]. Using this modal abundance yields a contribution by the CE5 impact glass beads to bulk soils of 4–78 $\mu g\,g^{-1}$ equivalent water, which is consistent with bulk water abundance estimates derived from reflectance spectroscopy measurements carried out from the CE5 lander[52]. Importantly, the major water-bearing phase in CE5 basalts is apatite in which water occurs as hydroxyl occupying the X site in apatite crystal structure[53,54]. The daily temperature variation of 93 K to 423 K
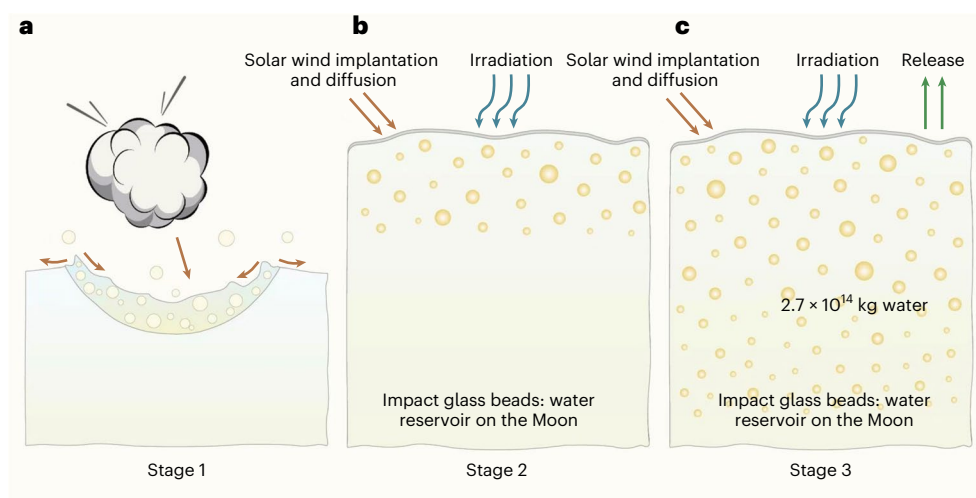
Fig. 4 | Schematic diagram of the lunar surface water cycle associated with impact glass beads. a, Because of the high temperature of formation of impact glass beads, most water present in precursor materials would have been lost. **b**, After their deposition at the surface, solar wind-derived water would diffuse into impact glass beads after solar wind H^{+} implantation. **c**, Gardening would transfer the impact glass beads deeper into the soils, creating a water reservoir at the subsurface of the Moon. The impact glass beads at the surface would still be able to release water into the lunar exosphere, due to meteoroid impact, for example[13]. The amount of water held by impact glass beads in lunar soils is estimated to be $0.03–27.00 \times 10^{13}$ kg, assuming a global depth of lunar soils of 3–12 m (refs. [56,57]), a modal abundance of impact glass beads in lunar soils of 3–5 vol.% (ref. [51]) and impact glass beads having a bulk H_2O abundance of 132–1,570 µg g^{-1}.

on the Moon's surface is not high enough to drive hydroxyl out from the apatite structure[32,55], indicating that impact glass beads are probably the dominant reservoir involved in the lunar surface water cycle, except for the space-weathered rims and possibly water ice in polar regions.

The global lunar surface is covered by lunar soils with a thickness ranging from about 3 m to 12 m (refs. [56,57]). The amount of water in lunar soils contributed by impact glass beads varies from 3.0×10^{11} kg to 2.7×10^{14} kg, based on the bulk water abundance of 132–1,570 µg g^{-1} in impact glass beads and a modal abundance of ~3–5 vol.% (ref. [51]) (Fig. 4). Importantly, this estimate provides a minimum quantity of water available at the lunar subsurface as it does not take into account the water contribution from permanently shadowed regions[4–6,11], indigenous lunar rocks (for example, ref. [26]), delivery by meteoritic impacts[13,27] and solar wind-derived water preserved in the space-weathered rims of lunar soils[34,35]. These findings indicate that the lunar soils contain a much higher amount of solar wind-derived water than previously thought, which could be a water reservoir for in situ utilization in future lunar exploration. Indeed, this water entrapped in impact glass beads appears to be quite easy to extract as shown by the post-diffusion de-gassing profile for bead CE5#33,036 (Fig. 3 and Methods).

Implications for water on airless bodies

Asteroid and comet impacts are the major exogenous processes that reshape the surface morphologies of airless bodies, as evidenced by the widespread presence of impact craters on the Moon[58], Mercury[59] and asteroids[60,61]. These impacts probably create impact glasses and glass beads on any airless bodies, as evidenced by the studies of lunar soils[62] and howardites[63]. This study demonstrates that impact glass beads have the capacity to store significant quantities of solar wind-derived water at the surface of airless bodies, in addition to the possible presence of water ice trapped in permanently shadowed areas in polar regions. The presence of water, stored in impact glass beads, is consistent with the remote detection of water at lower-latitude regions of the Moon[5–12], 4 Vesta[64] and Mercury[65,66]. Our findings indicate that the impact glasses on the surface of Solar System airless bodies are capable of storing solar wind-derived water and releasing it to space.

Online content

Any methods, additional references, Nature Portfolio reporting summaries, source data, extended data, supplementary information, acknowledgements, peer review information; details of author contributions and competing interests; and statements of data and code availability are available at https://doi.org/10.1038/s41561-023-01159-6.

References

1. Watson, K., Murray, B. & Brown, H. On the possible presence of ice on the Moon. *J. Geophys. Res.* **66**, 1598–1600 (1961).
2. Watson, K., Murray, B. C. & Brown, H. The behavior of volatiles on the lunar surface. *J. Geophys. Res.* **66**, 3033–3045 (1961).
3. Zeller, E. J., Ronca, L. B. & Levy, P. W. Proton-induced hydroxyl formation on the lunar surface. *J. Geophys. Res.* **71**, 4855–4860 (1966).
4. Feldman, W. C. et al. Fluxes of fast and epithermal neutrons from Lunar Prospector: evidence for water ice at the lunar poles. *Science* **281**, 1496–1500 (1998).
5. Pieters, C. M. et al. Character and spatial distribution of OH/H_2O on the surface of the Moon seen by M[3] on Chandrayaan-1. *Science* **326**, 568–572 (2009).
6. Clark, R. N. Detection of adsorbed water and hydroxyl on the Moon. *Science* **326**, 562–564 (2009).
7. Sunshine, J. M. et al. Temporal and spatial variability of lunar hydration as observed by the Deep Impact spacecraft. *Science* **326**, 565–568 (2009).
8. Li, S. & Milliken, R. E. Water on the surface of the Moon as seen by the Moon Mineralogy Mapper: distribution, abundance, and origins. *Sci. Adv.* **3**, e1701471 (2017).
9. Bandfield, J. L., Poston, M. J., Klima, R. L. & Edwards, C. S. Widespread distribution of OH/H_2O on the lunar surface inferred from spectral data. *Nat. Geosci.* **11**, 173–177 (2018).
10. Wohler, C., Grumpe, A., Berezhnoy, A. A. & Shevchenko, V. V. Time-of-day-dependent global distribution of lunar surficial water/hydroxyl. *Sci. Adv.* **3**, e1701286 (2017).
11. Colaprete, A. et al. Detection of water in the LCROSS ejecta plume. *Science* **330**, 463–468 (2010).

12. Mitrofanov, I. G. et al. Hydrogen mapping of the lunar south pole using the LRO neutron detector experiment LEND. *Science* **330**, 483–486 (2010).

13. Benna, M., Hurley, D. M., Stubbs, T. J., Mahaffy, P. R. & Elphic, R. C. Lunar soil hydration constrained by exospheric water liberated by meteoroid impacts. *Nat. Geosci.* **12**, 333–338 (2019).

14. Honniball, C. I. et al. Molecular water detected on the sunlit Moon by SOFIA. *Nat. Astron.* **5**, 121–127 (2021).

15. McCord, T. B. et al. Sources and physical processes responsible for OH/H_2O in the lunar soil as revealed by the Moon Mineralogy Mapper (M^3). *J. Geophys. Res.* **116**, E00G05 (2011).

16. Schaible, M. J. & Baragiola, R. A. Hydrogen implantation in silicates: the role of solar wind in SiOH bond formation on the surfaces of airless bodies in space. *J. Geophys. Res. Planets* **119**, 2017–2028 (2014).

17. Schörghofer, N. Migration calculations for water in the exosphere of the Moon: dusk–dawn asymmetry, heterogeneous trapping, and D/H fractionation. *Geophys. Res. Lett.* **41**, 4888–4893 (2014).

18. Farrell, W. M., Hurley, D. M. & Zimmerman, M. I. Solar wind implantation into lunar regolith: hydrogen retention in a surface with defects. *Icarus* **255**, 116–126 (2015).

19. Jones, B. M., Aleksandrov, A., Hibbitts, K., Dyar, M. D. & Orlando, T. M. Solar wind-induced water cycle on the Moon. *Geophys. Res. Lett.* **45**, 10959–10967 (2018).

20. Tucker, O. J., Farrell, W. M., Killen, R. M. & Hurley, D. M. Solar wind implantation into the lunar regolith: Monte Carlo simulations of H retention in a surface with defects and the H_2 exosphere. *J. Geophys. Res. Planets* **124**, 278–293 (2019).

21. Saal, A. E. et al. Volatile content of lunar volcanic glasses and the presence of water in the Moon's interior. *Nature* **454**, 192–195 (2008).

22. Tartèse, R. et al. The abundance, distribution, and isotopic composition of hydrogen in the Moon as revealed by basaltic lunar samples: implications for the volatile inventory of the Moon. *Geochim. Cosmochim. Acta* **122**, 58–74 (2013).

23. Hui, H. J. et al. Cooling rates of lunar orange glass beads. *Earth Planet. Sci. Lett.* **503**, 88–94 (2018).

24. Milliken, R. E. & Li, S. Remote detection of widespread indigenous water in lunar pyroclastic deposits. *Nat. Geosci.* **10**, 561–565 (2017).

25. Hui, H. J., Peslier, A. H., Zhang, Y. X. & Neal, C. R. Water in lunar anorthosites and evidence for a wet early Moon. *Nat. Geosci.* **6**, 177–180 (2013).

26. Greenwood, J. P. et al. Hydrogen isotope ratios in lunar rocks indicate delivery of cometary water to the Moon. *Nat. Geosci.* **4**, 79–82 (2011).

27. Liu, Y. et al. Direct measurement of hydroxyl in the lunar regolith and the origin of lunar surface water. *Nat. Geosci.* **5**, 779–782 (2012).

28. Füri, E., Deloule, E., Gurenko, A. & Marty, B. New evidence for chondritic lunar water from combined D/H and noble gas analyses of single Apollo 17 volcanic glasses. *Icarus* **229**, 109–120 (2014).

29. Joy, K. H. et al. The isotopic composition of volatiles in the unique Bench Crater carbonaceous chondrite impactor found in the Apollo 12 regolith. *Earth Planet. Sci. Lett.* **540**, 116265 (2020).

30. Housley, R., Grant, R. & Paton, N. Origin and characteristics of excess Fe metal in lunar glass welded aggregates. *Proc. Lunar Sci. Conf.* **4**, 2737–2749 (1973).

31. Managadze, G. G., Cherepin, V. T., Shkuratov, Y. G., Kolesnik, V. N. & Chumikov, A. E. Simulating OH/H_2O formation by solar wind at the lunar surface. *Icarus* **215**, 449–451 (2011).

32. Li, S. & Milliken, R. E. An empirical thermal correction model for Moon Mineralogy Mapper data constrained by laboratory spectra and Diviner temperatures. *J. Geophys. Res. Planet.* **121**, 2081–2107 (2016).

33. Jones, B. M., Aleksandrov, A., Hibbitts, C. A. & Orlando, T. M. Thermal evolution of water and hydrogen from Apollo lunar regolith grains. *Earth Planet. Sci. Lett.* **571**, 117107 (2021).

34. Zhou, C. et al. Chang'e-5 samples reveal high water content in lunar minerals. *Nat. Commun.* **13**, 5336 (2022).

35. Xu, Y. et al. High abundance of solar wind-derived water in lunar soils from the middle latitude. *Proc. Natl Acad. Sci. USA* **119**, e2214395119 (2022).

36. Saal, A. E., Hauri, E. H., Van Orman, J. A. & Rutherford, M. J. Hydrogen isotopes in lunar volcanic glasses and melt inclusions reveal a carbonaceous chondrite heritage. *Science* **340**, 1317–1320 (2013).

37. Morris, R. V. *Handbook of Lunar Soils* (Lyndon B. Johnson Space Center, 1983).

38. Li, C. et al. Characteristics of the lunar samples returned by the Chang'e-5 mission. *Natl Sci. Rev.* **9**, nwab188 (2022).

39. Long, T. et al. Constraining the formation and transport of lunar impact glasses using the ages and chemical compositions of Chang'e-5 glass beads. *Sci. Adv.* **8**, eabq2542 (2022).

40. Hashizume, K., Chaussidon, M., Marty, B. & Robert, F. Solar wind record on the moon: deciphering presolar from planetary nitrogen. *Science* **290**, 1142–1145 (2000).

41. Epstein, S. & Taylor, H. P. Jr. The isotopic composition and concentration of water, hydrogen, and carbon in some Apollo 15 and 16 soils and in the Apollo 17 orange soil. *Proc. Lunar Sci. Conf.* **4**, 1559–1575 (1973).

42. Tartèse, R. et al. Apatites in lunar KREEP basalts: the missing link to understanding the H isotope systematics of the Moon. *Geology* **42**, 363–366 (2014).

43. Robert, F., Gautier, D. & Dubrulle, B. The solar system D/H ratio: observations and theories. *Space Sci. Rev.* **92**, 201–224 (2000).

44. Alexander, C. M. et al. The provenances of asteroids, and their contributions to the volatile inventories of the terrestrial planets. *Science* **337**, 721–723 (2012).

45. Altwegg, K. et al. Cometary science. 67P/Churyumov-Gerasimenko, a Jupiter family comet with a high D/H ratio. *Science* **347**, 1261952 (2015).

46. Hartogh, P. et al. Ocean-like water in the Jupiter-family comet 103P/Hartley 2. *Nature* **478**, 218–220 (2011).

47. Jones, B. M., Aleksandrov, A., Dyar, M. D., Hibbitts, C. A. & Orlando, T. M. Investigation of water interactions with Apollo lunar regolith grains. *J. Geophys. Res. Planet.* **125**, e06147 (2020).

48. Zouine, A., Dersch, O., Walter, G. & Rauch, F. Diffusivity and solubility of water in silica glass in the temperature range 23–200 °C. *Phys. Chem. Glasses B* **48**, 85–91 (2007).

49. Hauri, E. et al. SIMS analysis of volatiles in silicate glasses. *Chem. Geol.* **183**, 99–114 (2002).

50. Hu, S. et al. A dry lunar mantle reservoir for young mare basalts of Chang'e-5. *Nature* **600**, 49–53 (2021).

51. McKay, D. S. et al. The lunar regolith in *Lunar sourcebook* Ch. 7, 285–356 (Cambridge Univesity Press, 1991).

52. Lin, H. et al. In situ detection of water on the Moon by the Chang'E-5 lander. *Sci. Adv.* **8**, eabl9174 (2022).

53. Boyce, J. W., Tomlinson, S. M., McCubbin, F. M., Greenwood, J. P. & Treiman, A. H. The lunar apatite paradox. *Science* **344**, 400–402 (2014).

54. McCubbin et al. Experimental investigation of F, Cl, and OH partitioning between apatite and Fe-rich basaltic melt at 1.0–1.2 GPa and 950–1000 °C. *Am. Mineral.* **4779**, 83–89 (2015).

55. Ingrin, J. & Blanchard, M. Diffusion of hydrogen in minerals. *Rev. Mineral. Geochem.* **62**, 291–320 (2006).

56. Zhang, J. et al. Volcanic history of the Imbrium basin: a close-up view from the lunar rover Yutu. *Proc. Natl Acad. Sci. USA* **112**, 5342–5347 (2015).

57. Zhang, J. et al. Lunar regolith and substructure at Chang'e-4 landing site in south pole–Aitken basin. *Nat. Astron.* **5**, 25–30 (2020).

58. Head, J. W. 3rd et al. Global distribution of large lunar craters: implications for resurfacing and impactor populations. *Science* **329**, 1504–1507 (2010).

59. Strom, R. G., Chapman, C. R., Merline, W. J., Solomon, S. C. & Head, J. W. 3rd Mercury cratering record viewed from MESSENGER's first flyby. *Science* **321**, 79–81 (2008).

60. Jaumann, R. et al. Vesta's shape and morphology. *Science* **336**, 687–690 (2012).

61. Abe, S. et al. Mass and local topography measurements of Itokawa by Hayabusa. *Science* **312**, 1344–1347 (2006).

62. Taylor, G. J. et al. Modal analyses of lunar soils by quantitative X-ray diffraction analysis. *Geochim. Cosmochim. Acta* **266**, 17–28 (2019).

63. Singerling, S. A., McSween, H. Y. Jr. & Taylor, L. A. Glasses in howardites: impact melts or pyroclasts? *Meteorit. Planet. Sci.* **48**, 715–729 (2013).

64. Prettyman, T. H. et al. Elemental mapping by Dawn reveals exogenic H in Vesta's regolith. *Science* **338**, 242–246 (2012).

65. Harmon, J. K. & Slade, M. A. Radar mapping of Mercury: full-disk images and polar anomalies. *Science* **258**, 640–643 (1992).

66. Lawrence, D. J. et al. Evidence for water ice near Mercury's north pole from MESSENGER neutron spectrometer measurements. *Science* **339**, 292–296 (2013).

Methods

Sample preparation

The CE5 lunar soil allocated by the China National Space Administration and used in this study is CE5C0100YJFM00103, weighing ~1 g. The CE5 lunar soils were scooped by the robotic arm on board the CE5 lander. A total of 150 individual grains, varying in size from ~50 μm to ~1 mm in diameter, were hand picked under a binocular microscope in the ultraclean room at the Institute of Geology and Geophysics, Chinese Academy of Sciences (IGGCAS). The hand-picked grains were mounted in epoxy and prepared as a double polished section with a thickness of about 100 μm (Supplementary Fig. 1 and Supplementary Table 1). The surrounding epoxy was removed to improve the vacuum quality for the water abundance measurements using NanoSIMS[67]. The prepared section was cleaned using anhydrous ethanol before drying at 60 °C in a baking oven overnight.

SEM observation

Petrographic observations were carried out using field-emission SEM using FEI Nova NanoSEM 450 and Thermofisher Apreo instruments at the IGGCAS, using electron beam currents of 2.0–6.4 nA and an acceleration voltage of 15 kV. The prepared sections were initially coated with carbon for petrographic observations and analyses of mineral chemistry and then recoated with Au for in situ NanoSIMS measurement of water content and hydrogen isotopes. After NanoSIMS analyses, Au coating was removed, and the samples were recoated with carbon and observed by SEM to confirm the positions of the NanoSIMS spots.

Electron probe microanalysis

Before the NanoSIMS analyses, we used the CAMECA SXFive EPMA at IGGCAS to quantify the major and minor elemental abundances in CE5 impact glass beads. The operating accelerating voltage was 20 kV and the beam current was 10 nA, with a 10 μm beam diameter. The total counting time was 10 min for each analysis. One basalt glass (VG-2) and one komatiite glass (MPI-DING-GOR128) were used to monitor the analysis accuracy and precision[68]. The detection limits were (3σ) 0.02 wt% for Na, Ni, K, S and P, 0.04 wt% for Ca, 0.05 wt% for Al, Mg and Cr, 0.06 wt% for Si and Ti and 0.09 wt% for Mn and Fe. The EPMA data obtained for impact glass beads are listed in Supplementary Table 2.

In situ water abundance and hydrogen isotope analyses

Two analytical sessions were designed to measure the water abundances and hydrogen isotope compositions of CE5 impact glass beads using a CAMECA NanoSIMS 50L at the IGGCAS. In the first session, measurements at the cores and rims of CE5 impact glass beads were carried out to investigate the potential water zonation features in the glasses. In the second session, more-detailed profile measurements on five individual CE5 impact glasses were acquired, as well as several parallel measurements on other glass beads for cross checking. A liquid nitrogen cold trap was used to further improve the vacuum quality in the second session.

The sample and the standard prepared in different mounts were loaded in the same sample holder of NanoSIMS and were baked overnight at ~60 °C in the NanoSIMS airlock. The holders were then stored in the NanoSIMS sample chamber to improve the vacuum quality and minimize the H background[49,67]. The vacuum pressure in the analysis chamber was 1.5×10^{-10} to 1.9×10^{-10} Torr during analysis. Each 7 μm × 7 μm analysis area was pre-sputtered for 2 min with a Cs^+ ion beam current of 2 nA to remove the surface coating and potential contamination. During analysis, the secondary anions $^1H^-$, $^2D^-$, $^{12}C^-$ and $^{18}O^-$ were simultaneously counted by electron multipliers (EMs) from the central 5 μm × 5 μm areas using the NanoSIMS electronic gate technique (49% blanking). A 44 ns dead time was corrected for all EMs, while the EM noise (<10^{-2} cps) was ignored. We used a primary ion

beam current of ~0.5 nA for analysis, corresponding to a beam size of ~500 nm in diameter. The charging effect on the sample surfaces was compensated by an electron gun during analysis.

A chip of the nominally anhydrous San Carlos olivine reference, with a reported water content of 1.4 μg g^{-1} (ref. [69]), was used for instrument H_2O background corrections, following the relationship $H/O_{bg} = (H_{counts} - H_{bg})/O_{counts}$ and $D/H_{measured} = (1 - f) \times D/H_{true} + f \times D/H_{bg}$, where f is the proportion of H emitted from the instrumental background[70]. In the first session, D/H_{bg} was 2.83 ($\pm$1.98) × 10^{-4} and $H_{bg} = 815 \pm 457$ cps (2 s.d., $N = 16$, corresponding to an instrument H_2O background abundance of 29.8 ± 14.8 μg g^{-1} (2 s.d.)). In the second session, the measured H counts on the central areas of CE5 impact glass beads are even lower than that of San Carlos olivine. Therefore, the extremely low H/O ratio measurements on CE5 impact glass beads were treated as reference ($H_{bg} = 215 \pm 40$ cps, corresponding to an instrument H_2O background of 11.7 ± 2 μg g^{-1}) for background correction.

After an instrument H_2O background subtraction, the water abundances of CE5 impact glass beads were calculated from the background-subtracted H/O ratios multiplied by the slope of the calibration lines (Extended Data Fig. 2), which were determined by measuring two apatite standards, Durango apatite ($H_2O = 0.0478$ wt% and $\delta D = -120 \pm 5$‰) (refs. [26,71]) and Kovdor apatite ($H_2O = 0.98 \pm 0.07$ wt% and $\delta D = -66 \pm 21$‰) (ref. [72]), the SWIFT mid-ocean-ridge basalt (MORB) glass ($H_2O = 0.258$ wt% and $\delta D = -73 \pm 2$‰) and two basaltic glasses, 519-4-1 ($H_2O = 0.17$ wt%) (ref. [49]) and 1833-11 ($H_2O = 1.2$ wt%) (ref. [49]) (Supplementary Table 3). Corrections for instrumental mass fractionation (IMF) on H isotopic compositions were carried out using repeated analyses of the SWIFT MORB glass standard and monitored by analysing both the Durango apatite and Kovdor apatite standards during the whole analytical session (Extended Data Fig. 3). The matrix effects on water abundance and IMF on hydrogen isotope composition are the same between apatite and silicate glass within analytical uncertainties[67]. Hydrogen isotopic compositions are given using the delta notation, $\delta D = ((D/H)_{sample}/(D/H)_{SMOW}) - 1) \times 1,000$‰, where SMOW is the standard mean ocean water with a D/H ratio of 1.5576×10^{-4}. More technical details can be found in ref. [67]. All data are reported with their 2 s.d. analytical uncertainties, which include reproducibility of D/H measurements on the reference materials, uncertainty of H_2O background subtraction and internal precision on each analysis (Supplementary Tables 3 and 4). The raw measured D/H ratios were corrected for the background, followed by correction for IMF.

Raman spectroscopy

The Raman spectra of impact glasses were collected using a WITec alpha 300 R confocal Raman system and carried out after the NanoSIMS measurements at the IGGCAS. An optical microscope with an objective of 0.9 NA and ×50 magnification was used to focus the Ar^+ laser beam with a 484 nm excitation wavelength on the target phases. Raman spectra were acquired with a total integration time of 500 s, a 9.2 mW laser power and a beam size of 5 μm. Three CE5 impact glass beads CE5#33,076 with water abundances zoning from 1,909 μg g^{-1} at the rims to <10 μg g^{-1} in the cores were chosen for Raman analyses (Extended Data Fig. 6). Along with the CE5 impact glass beads, terrestrial MORB glasses, MRN-G1 ($H_2O = 1.5$ wt%) (ref. [73]) and EPR-G3 ($H_2O = 0.22$ wt%)[73], were also measured to demonstrate the variation of Raman peak intensity of water and/or hydroxyl at ~3,300 cm^{-1} to 3,700 cm^{-1} with their water abundance (Extended Data Fig. 6).

Correction of water abundances and D/H ratios for spallation effects

The measured D/H ratios have been corrected for the potential effects of spallation by cosmic ray, using a D production rate of 2.17×10^{-12} mol g^{-1} Myr^{-1} (ref. [74]) for impact glasses. The correction errors induced by D spallation are around 5% on D/H ratios and negligible

on water content[36]. Because no cosmic-ray exposure age is yet available for the CE5 impact glass beads, a cosmic-ray exposure age of 50 Ma estimated by Hu et al.[50] was used for correction of spallation in this study (Supplementary Table 3). Another D production rate, of 9.2×10^{-13} mol g^{-1} Myr^{-1} (ref. [75]), was also used for correction of spallation effects to account for the suggestion that the D production rate of 2.17×10^{-12} mol g^{-1} Myr^{-1} (ref. [74]) may not be appropriate for impact glasses. As the D production rate in Ref. [75] is slower, corrections for spallation-produced D are even smaller, not making any notable difference overall for our analytical results (Supplementary Table 4).

De-gassing modelling

The hydrogen isotope fractionation during volatile loss into a vacuum is given by $\alpha^2 = M1/M2$, where $M1$ and $M2$ are the masses of the volatile phase isotopologues. The change of the isotopic composition of H during volatile loss by Rayleigh fractionation is given by $R = R_0 \times f^{(\alpha-1)}$, where R_0 and R are the initial and final D/H ratios for a fraction f of remaining hydrogen[76]. De-gassing of H$_2$ ($M1 = 2$ for H$_2$ and $M2 = 3$ for HD) yields an α value of ~0.8165 (ref. [76]) (Fig. 2). The de-gassing modelling assumes that the CE5 impact glass beads have an initial water abundance of 2,000 µg g^{-1}, an initial D/H ratio of 3.1×10^{-6} (corresponding to that of the analysis with the highest H$_2$O abundance) and de-gas in the form of H$_2$, yielding a δD value increase from −980‰ at $f = 1$ to −926‰ at $f = 0.001$.

Diffusion modelling

The five sharp hydration profiles of CE5 impact glass beads were simulated by a simplified diffusion process that follows Fick's second law as equation (1) (ref. [77]).

$$C(x) = (C_s - C_0)\,\mathrm{erfc}\left(\frac{x}{2\sqrt{Dt}}\right) + C_0 \qquad (1)$$

In equation 1, D is the diffusion coefficient that depends on temperature, x is the distance to the rim, C_0 is the initial water abundance of the CE5 impact glass beads, $C(x)$ is the water abundance at distance x, C_s is the maximum water abundance at the rims, t is duration of diffusion and erfc is the complementary error function.

Considering the scooped samples were collected from less than 3 cm deep[38], diffusion simulations were performed using a peak temperature of 360 K, relevant for a latitude of 45° N on the Moon[32], because the peak temperature is the main controlling factor for the diffusion time[35]. The H diffusion coefficients of water/hydroxyl (D_H) determined on silica glass[48], $D_H = 20.84$ µm^2 yr^{-1} at 360 K, were used in our simulations. It is not possible to reconstruct the orientation of the exposed surface of the studied impact glass beads on the lunar surface. Thus, we carried out a simplistic diffusion modelling based on the measured profiles, assuming a constant C_s at the rims for each bead based on their diverse Pb–Pb ages[39]. The diffusion duration is roughly a maximum constraint for qualitatively estimating the efficiency of solar wind-derived OH/H$_2$O recharged in impact glass beads. The water abundances at the rims (C_s) of the six CE5 impact glass bead profiles are extrapolated from the measured profiles using 2,000 µg g^{-1}, 2,000 µg g^{-1}, 1,600 µg g^{-1}, 500 µg g^{-1}, 2,600 µg g^{-1} and 3,000 µg g^{-1} and a C_0 of 10 µg g^{-1} for Profiles 1–6, respectively. The diffusional durations vary from 3.0 to 9.0 years, 5.0 to 15.0 years, 1.0 to 4.5 years, 2.0 to 6.0 years, 0.5 to 4.0 years and 2.0 to 14.0 years at $T = 360$ K for Profiles 1–6, respectively, based on the apparent distance (Fig. 1) and a fixed C_s at the rims for each profile.

For the notable post-diffusion de-gassing feature of Profile 2, a two-stage modelling of water diffusion (Stage 1) and post-diffusion de-gassing (Stage 2) was carried out to fit the measured water abundance profile. The water-diffusion details in Stage 1 have been described in the preceding. A post-diffusion de-gassing of water (Stage 2) was modelled to fit the bell shape of water abundance on the right side

(Fig. 3). The water abundance on the right side modelled in Stage 1 was taken as the initial condition for modelling of Stage 2. The de-gassing rate is assumed to be proportional to the surface water abundance along the profile, where transmission capacity of a boundary was formulated as an additional boundary condition for the diffusion equation (see ref. [35] for more details). The corresponding δD profiles are calculated by a binary mixing model (Two-endmember mixing modelling) considering a limited diffusional fractionation for H isotope[78] compared with the large difference in δD values for the two endmembers (δD ≈ −980‰, D/H = 3.0×10^{-6} for solar wind-derived water and δD ≈ 500‰, D/H = 230×10^{-6} for the initial water in impact glass beads).

Two-endmember mixing modelling

In the two-endmember mixing model, the solar wind endmember is set to have a δD value of −980‰ (ref. [41]) and a water abundance of 2,000 µg g^{-1}, which corresponds to the maximum measured value in this work (Fig. 2). The initial water component in CE5 impact glass beads could have a minimum δD value of ~500‰ based on the measurements on CE5 apatite[50], yielding a best fit of initial water abundance of 5–50 µg g^{-1} before the addition of solar wind-derived water (Fig. 2). On the basis of the following mass balance (equations (2) and (3)), we can model the relationship between the measured water abundances and δD values:

$$H_2O_0 + H_2O_{solar} = H_2O_{measured} \qquad (2)$$

$$H_2O_0 \times D/H_0 + H_2O_{solar} \times D/H_{solar} = H_2O_{measured} \times D/H_{measured} \qquad (3)$$

where H$_2$O$_0$ and D/H$_0$ are the initial water abundance and D/H ratio of CE5 impact glass beads before the addition of solar wind-derived water, respectively, H$_2$O$_{solar}$ is the water abundance contributed by solar wind-derived water, D/H$_{solar}$ is the hydrogen isotopic composition of solar wind-derived water, and H$_2$O$_{measured}$ and D/H$_{measured}$ are the water abundance and D/H ratio measured from CE5 impact glass beads, respectively.

Petrography and chemistry of CE5 impact glass beads

Petrography. A total of 150 impact glass fragments were mounted in CE5#33 mount (Supplementary Fig. 1 and Supplementary Table 1). There are 117 glass fragments displaying ovoid to spherical shapes, which are mainly composed mainly of glass, 1 glass rod, 3 olivine and plagioclase monomict clasts, 1 basaltic fragment and 28 glass fragments showing irregular shapes, which are composed mainly of glass, mafic mineral fragments and large bubbles (Supplementary Fig. 1 and Supplementary Table 1). The ovoid to spherical fragments are referred to as glass beads in this work and further classified into two textural types, homogeneous and heterogeneous glass beads (Fig. 1, Supplementary Fig. 2 and Supplementary Table 1). The homogeneous glass beads display smooth surfaces and homogeneous contrast in back-scattered electron images while the heterogeneous glass beads usually contain some vesicles, pyroxene and plagioclase clasts and micrometre-sized sulfide spheres (Fig. 1 and Supplementary Fig. 2). The textural differences between homogeneous and heterogeneous glass beads could reflect a higher formation temperature for the homogeneous glass beads (Fig. 1 and Supplementary Fig. 2).

Chemistry. A total of 32 homogeneous impact glass beads were selected for EPMA analyses. The analytical results are listed in Supplementary Table 2. The analysed glass beads have a mare origin, except for two glass beads plotting in the highlands population and another two distributed in pyroclastic areas judging from their CaO/Al$_2$O$_3$ and MgO/Al$_2$O$_3$ ratios (Extended Data Fig. 1)[79,80]. These glasses plotting in non-mare fields are not discussed further in this work because their origin is currently uncertain. The homogeneous

CE5 impact glass beads are composed mainly of SiO_2 (31.2–44.5 wt%), TiO_2 (3.95–6.54 wt%), Al_2O_3 (10.4–17.3 wt%), FeO (17.6–23.5 wt%), MgO (5.94–10.9 wt%) and CaO (10.1–15.4 wt%), with minor Cr_2O_3 (0.12–0.28 wt%), MnO (0.22–0.31 wt%), NiO (0.15–0.61 wt%), Na_2O (<0.17 wt%, most <0.05 wt%) and K_2O (<0.06 wt%) (Supplementary Table 2). Each single glass bead is homogeneous in terms of its major element chemical composition (Supplementary Table 2). Most CE5 homogeneous impact glass beads have compositions similar to the bulk CE5 basalt compositions reported by refs. [38,81], indicating that they could have been formed locally rather than ejected from other regions. This prediction is consistent with the similar geochemical characteristics between CE5 impact glass beads and CE5 bulk basalts[82]. The Pb–Pb dating of the CE5 impact glass beads indicates that they were formed in the range of 4–2,000 Ma by various local meteoritic impacts[39].

Water abundances and hydrogen isotope compositions of the CE5 impact glass beads

A total of 32 CE5 impact glass beads with smooth exposed surface (Fig. 1 and Supplementary Fig. 2) and a mare origin (Extended Data Fig. 2) were selected for the NanoSIMS measurements of water abundances and hydrogen isotopic compositions. In the first analytical session, the objective was to investigate the homogeneity of water abundance within each glass bead; therefore, two analyses of the cores and the rims on relatively large glass beads were carried out to identify the hydration and or de-gassing candidate profiles. In the second session, six more-detailed profile analyses were carried out on five CE5 impact glass beads (Fig. 1), as well as several duplicate measurements on other glass beads (Supplementary Fig. 2). Overall, the analytical water abundances in the first session are in the range of the second session due to the heterogeneous distribution of water in the CE5 impact glass beads (Fig. 2 and Supplementary Table 4). The water abundances of the analysed CE5 impact glass beads vary from ~0 to 1,909 μg g^{-1} and are negatively correlated with their δD values (−990 ± 6‰ to +522 ± 440‰) (Fig. 2 and Supplementary Table 4). Water abundances measured in all CE5 impact glass beads display higher values at the rims and decrease towards the glass bead cores (Fig. 3 and Extended Data Figs. 4 and 5). The δD values display the reverse trends (Fig. 3 and Extended Data Figs. 4 and 5). Three profile measurements (Profile 3, Profile 4 and Profile 5) show a sharp decrease in water abundance from the rim towards the core (Fig. 3 and Extended Data Figs. 4 and 5), while the other three (Profile 1, Profile 2 and Profile 6) display a modest decrease of water abundance towards the cores (Fig. 3 and Extended Data Figs. 4 and 5). It is also noticeable that the latter profiles have higher water abundances (1,055–1,909 μg g^{-1}) at the rim than do the former profiles (176–1,423 μg g^{-1}) (Fig. 3, Extended Data Figs. 4 and 5 and Supplementary Table 4). All of the profile measurements acquired on the central areas of CE5 impact glass beads have water abundances comparable to the instrument H_2O background (Supplementary Tables 3 and 4).

Data availability

All geochemical data generated in this study are included in Supplementary Tables 1–5 and are available via Zenodo (https://doi.org/10.5281/zenodo.7660603).

References

67. Hu, S. et al. Measurements of water content and D/H ratio in apatite and silicate glasses using a NanoSIMS 50L. *J. Anal. At. Spectrom.* **30**, 967–978 (2015).
68. Zhang, D. et al. High-precision measurement of trace level Na, K, P, S, Cr, and Ni in lunar glass using electron probe microanalysis. *At. Spectrosc.* **43**, 28–41 (2022).
69. Zhang, W. F. et al. Optimization of SIMS analytical parameters for water content measurement of olivine. *Surf. Interface Anal.* **52**, 224–233 (2019).
70. Tartèse, R., Anand, M. & Franchi, I. A. H and Cl isotope characteristics of indigenous and late hydrothermal fluids on the differentiated asteroidal parent body of Grave Nunataks 06128. *Geochim. Cosmochim. Acta* **266**, 529–543 (2019).
71. Greenwood, J. P., Itoh, S., Sakamoto, N., Vicenzi, E. P. & Yurimoto, H. Hydrogen isotope evidence for loss of water from Mars through time. *Geophys. Res. Lett.* **35**, L05203 (2008).
72. Nadeau, S. L., Epstein, S. & Stolper, E. Hydrogen and carbon abundances and isotopic ratios in apatite from alkaline intrusive complexes, with a focus on carbonatites. *Geochim. Cosmochim. Acta* **63**, 1837–1851 (1999).
73. Shimizu, K. et al. H_2O, CO_2, F, S, Cl, and P_2O_5 analyses of silicate glasses using SIMS: report of volatile standard glasses. *Geochem. J.* **51**, 299–313 (2017).
74. Füri, E., Deloule, E. & Trappitsch, R. The production rate of cosmogenic deuterium at the Moon's surface. *Earth Planet. Sci. Lett.* **474**, 76–82 (2017).
75. Merlivat, L., Leiu, M., Neif, G. & Roth, E. Spallation deuterium in rock 70215. In *7th Proc. Lunar Sci. Conf*, 649–658 (1976).
76. Sharp, Z. D., McCubbin, F. M. & Shearer, C. K. A hydrogen-based oxidation mechanism relevant to planetary formation. *Earth Planet. Sci. Lett.* **380**, 88–97 (2013).
77. Crank, J. *The Mathematics of Diffusion* (Oxford Univ. Press, 1975).
78. Graham, C. M. Experimental hydrogen isotope studies III: diffusion of hydrogen in hydrous minerals, and stable isotope exchange in metamorphic rocks. *Contrib. Mineral. Petrol.* **76**, 216–228 (1981).
79. Delano, J. W. Pristine lunar glasses: criteria, data, and implications. *Proc. Lunar Sci. Conf.* **91**, D201–D213 (1986).
80. Naney, M., Crowl, D. & Papike, J. The Apollo 16 drill core: statistical analysis of glass chemistry and the characterization of a high alumina-silica poor (HASP) glass. In *7th Proc. Lunar Sci. Conf.*, 155–184 (1976).
81. Tian, H. C. et al. Non-KREEP origin for Chang'e-5 basalts in the Procellarum KREEP Terrane. *Nature* **600**, 59–63 (2021).
82. Yang, W. et al. Geochemistry of impact glasses in the Chang'e-5 regolith: constraints on impact melting and the petrogenesis of local basalt. *Geochim. Cosmochim. Acta* **335**, 183–196 (2022).
83. Hu, S. et al. NanoSIMS analyses of apatite and melt inclusions in the GRV 020090 Martian meteorite: hydrogen isotope evidence for recent past underground hydrothermal activity on Mars. *Geochim. Cosmochim. Acta* **140**, 321–333 (2014).

Author contributions

S.H. and H. Hui designed this research. Huicun He, J.J., Y.Z., H.T., C.Z., L.G., J.L., D.Z., Q.M., L.J., Xiaoguang Li, Y.C., S.W., H.W., Q.L. and

Extended Data Fig. 1 | MgO/Al$_2$O$_3$ versus CaO/Al$_2$O$_3$ for the studied CE5 impact glass beads. Most smooth and homogeneous CE5 glass beads plot in the mare domain (Supplementary Table 2). Literature data for lunar impact and pyroclastic glasses in Apollo samples, Luna samples, and lunar meteorites (LMs) are from MoonDB (http://search.moondb.org) and are shown for comparison. Compositions of the CE5 bulk basalts and bulk soils (shaded yellow square) are from Tian et al.[81] and Li et al.[38]. Classification of lunar glasses (dashed lines) is from Refs. [79,80].
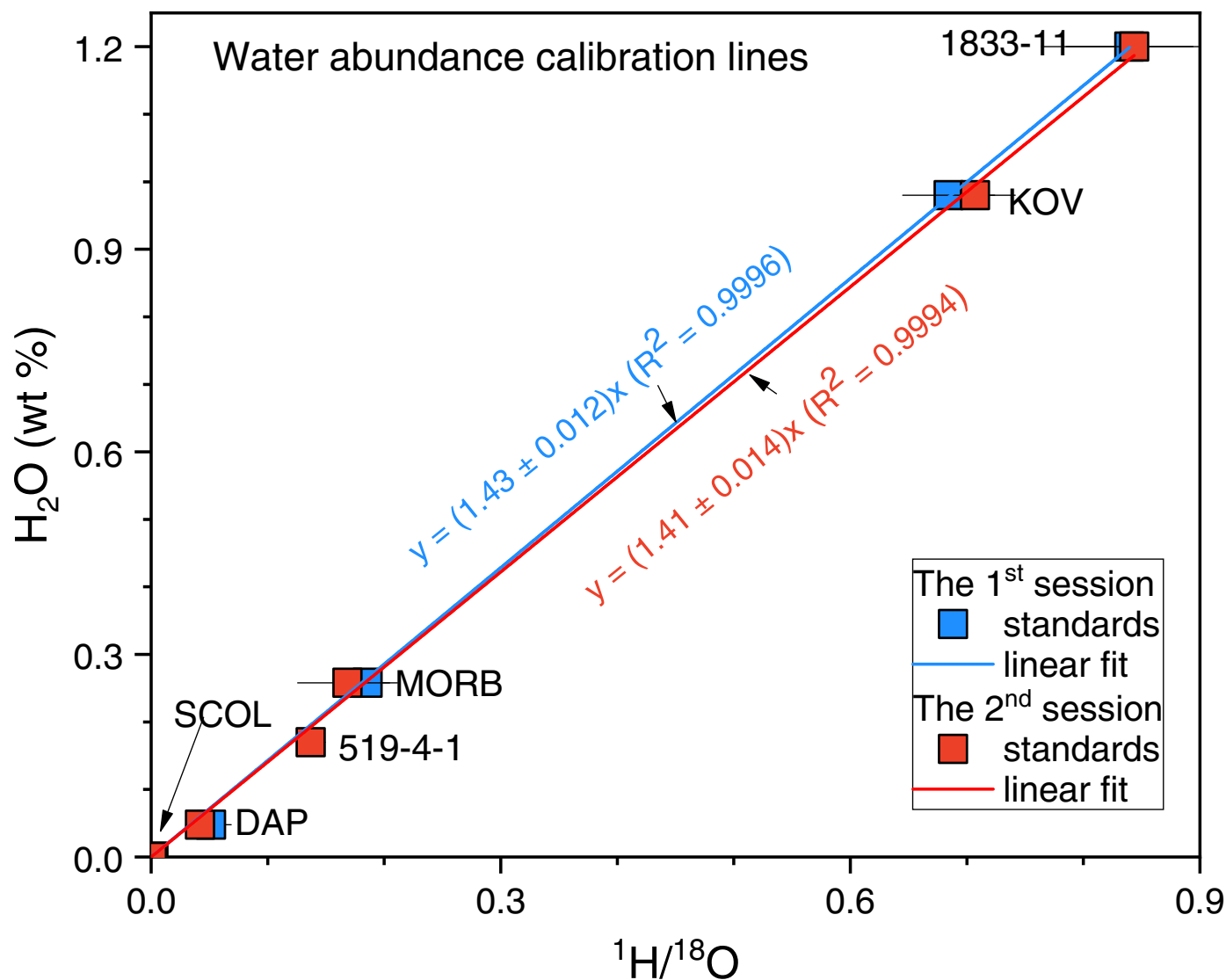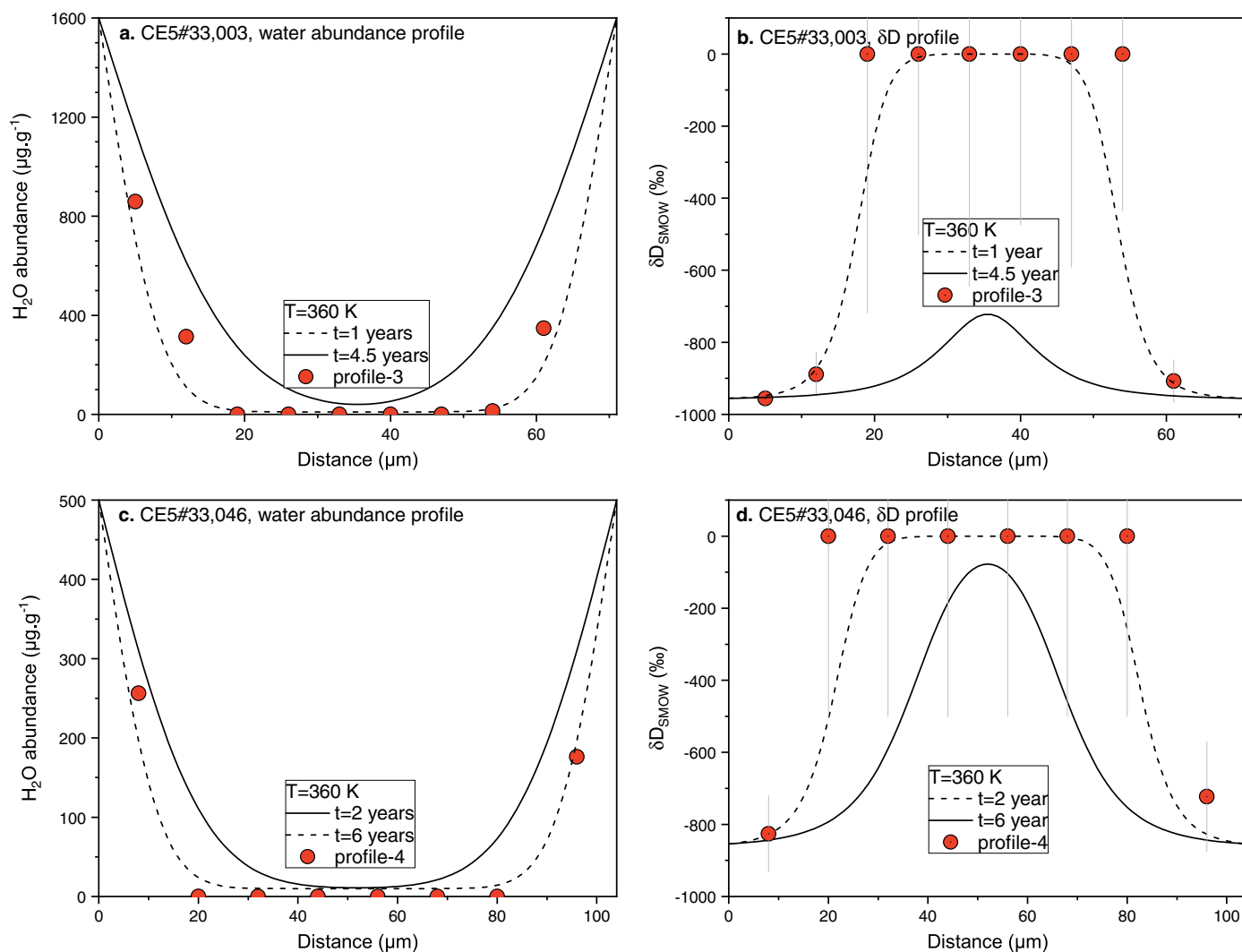
Extended Data Fig. 2 | The water abundance calibration lines established on standards. The linear slopes of the two analytical sessions are comparable and consistent with the slope of the instrument's long-term stability[50,67,83]. The analytical uncertainty is 1.7% (2σ) for the 1st session and 2.0% (2σ) for the 2nd session. The error bars are 2σ. KOV: Kovdor apatite, DAP: Durango apatite, SCOL: San Carlos olivine.
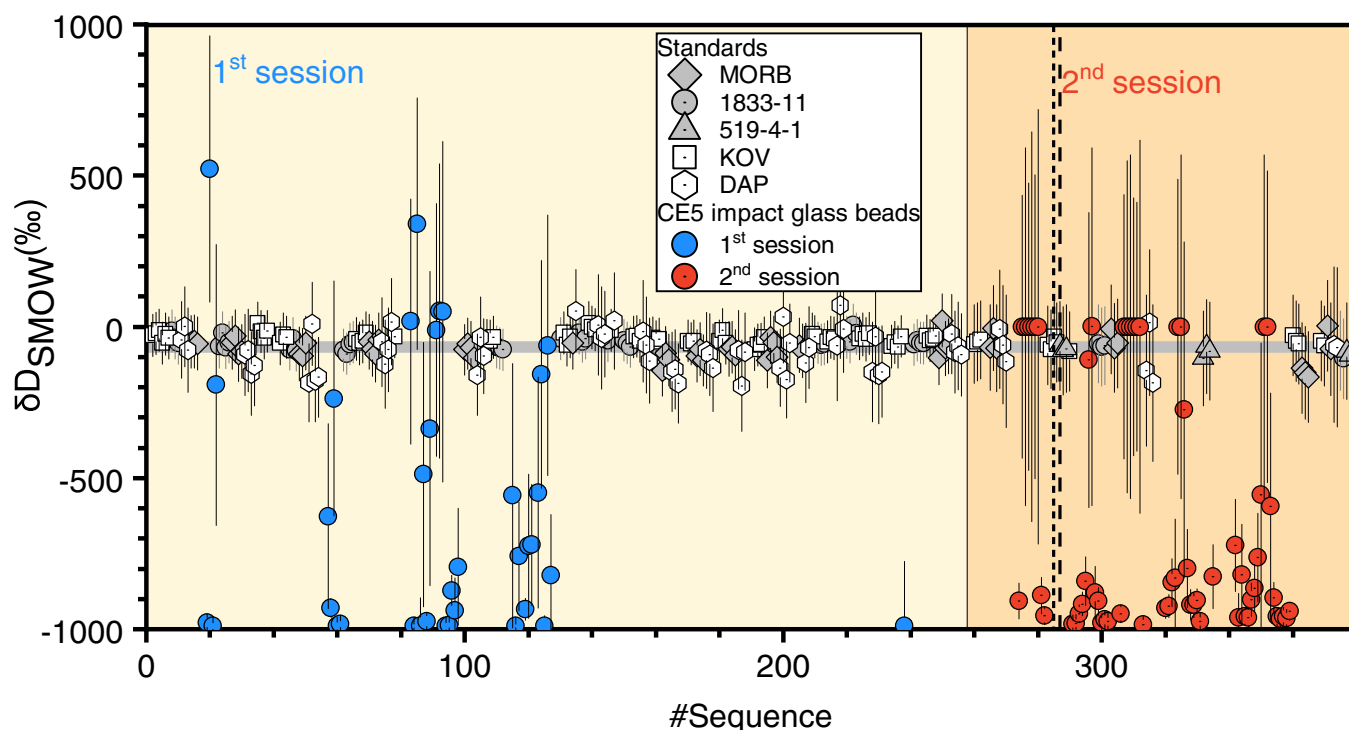
Extended Data Fig. 3 | Hydrogen isotope analysis sequences for the two analytical sessions. Analysis sequences are shown to monitor the reproducibility of hydrogen isotope analysis of the standards. δD values of Kovdor apatite (KOV), Durango apatite (DAP), SWIFT MORB (MORB), 1833-11, and 519-4-1 have been corrected for instrumental mass fractionation. And the fractionation factor (α_{IMF}) was established by SWIFT MORB glass. The reproducibility of δD analysis throughout the whole analytical session-1 and −2 are 58 ‰ (N = 38) and 117 ‰ (N = 11) (2σ), estimated by repeated analyses of the SWIFT MORB glass standard. The average δD values calculated for the Kovdor and Durango apatite are −39 ± 37 ‰ and −80 ± 134 ‰ (Supplementary Table 3), respectively, consistent with their recommended values within analytical errors[26,71]. The average δD values measured for the basaltic glass standards 1833-11 and 519-4-1 are −54 ± 42 ‰ and −80 ± 28 ‰ (Supplementary Table 3), respectively, which is consistent with the δD values reported in our previous work[50]. The error bars are 2 SD.

Extended Data Fig. 4 | Two zoning profiles of water abundances and δD values for CE5 impact glass beads (profile-3 on CE5#33,003 and profile-4 on CE5#33,046). a. water abundance profile on CE5#33,003. **b.** δD profile on CE5#33,003. **c.** water abundance profile on CE5#33,046. **d.** δD profile on CE5#33,046. The analytical locations of profile-3 on CE5#33,003 and profile-4 on CE5#33,046 are shown in Fig. 1. Hydroxyl/water diffusion modelling results at 360 K are shown in black lines. The diffusional durations vary from 1 to 4.5 years an 2 to 6 years for profile-3 and −4, respectively. For modelling details see Methods. The error bars are 2 SD.
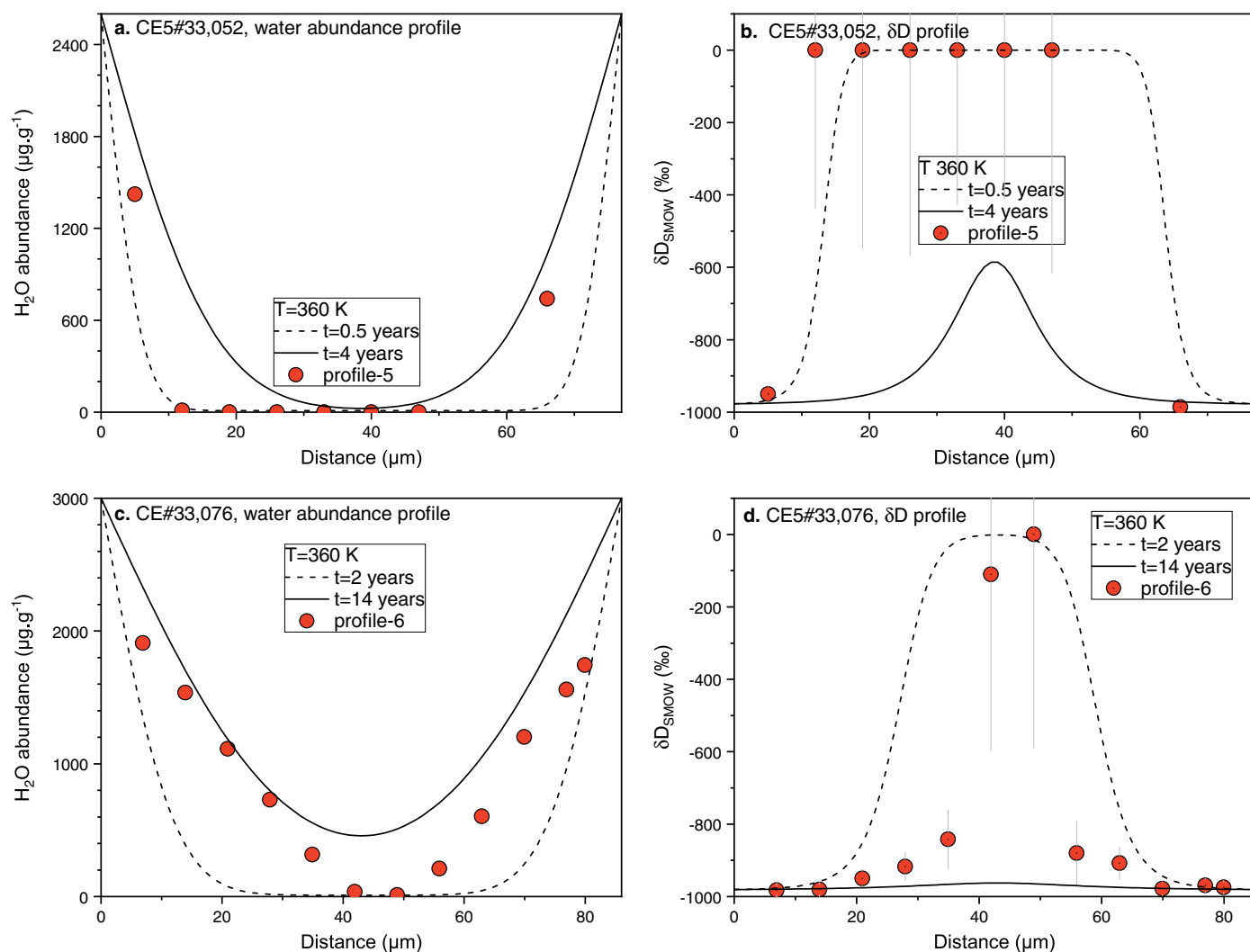
Extended Data Fig. 5 | Another two zoning profiles of water abundances and δD values for two CE5 impact glass beads (profile-5 on CE5#33,052 and profile-6 on CE5#33,076). a. water abundance profile on CE5#33,052. **b.** δD profile on CE5#33,052. **c.** water abundance profile on CE5#33,076. **d.** δD profile on CE5#33,076. The analytical locations of profile-3 and profile-4 are shown in Fig. 1. The diffusional durations vary from 0.5 to 4 years and 2 to 14 years at 360 K for profile-5 and −6, respectively. For modelling details see Methods. The error bars are 2 SD.
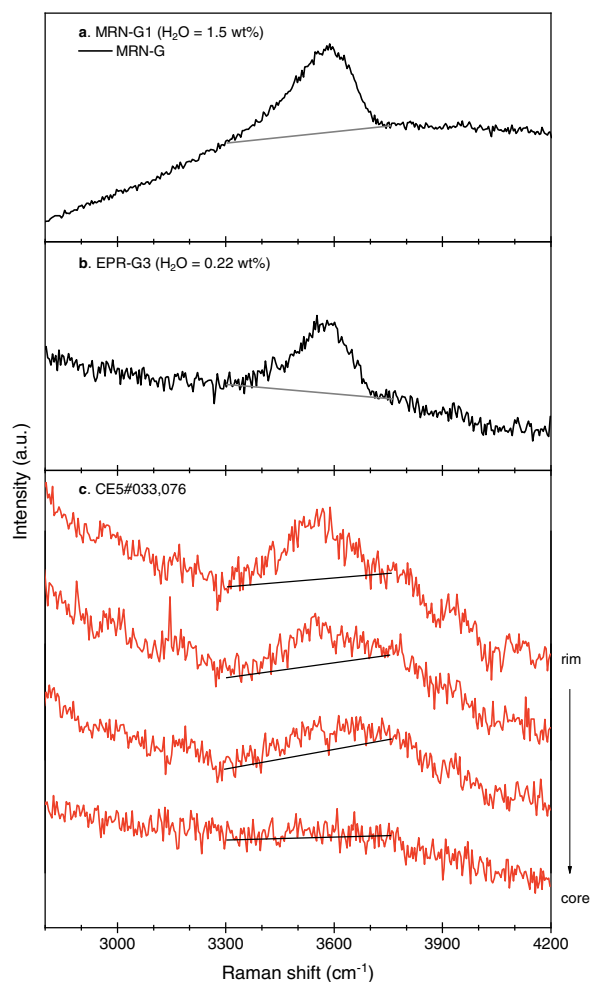
Extended Data Fig. 6 | Raman spectra. a,b, MORB glasses MRN-G1 (**a**) and EPR-G3 (**b**). **c**, CE5 impact glass bead, CE5#33,076. Raman peak at ~3500 cm^{-1} is ascribed to hydroxyl/molecular water. The grey lines are apparent baseline of the Raman peak between ~3300 and 3700 cm^{-1}. A notable H_2O zoning CE5 impact glass bead (CE5#33, 076) measured by NanoSIMS was chosen for Raman profile analysis. The Raman analytical positions of CE5 impact glass beads are outlined in Supplementary Fig. 2.